University of Reading

Adsorption of methyl acetoacetate at Ni{111}: experiment and theory

Article

Accepted Version

Ontaneda, J., Nicklin, R. E. J., Cornish, A., Roldan, A., Grau-Crespo, R. ORCID: https://orcid.org/0000-0001-8845-1719 and Held, G. (2016) Adsorption of methyl acetoacetate at Ni{111}: experiment and theory. Journal of Physical Chemistry C, 120 (48). pp. 27490-27499. ISSN 1932-7455 doi: 10.1021/acs.jpcc.6b10023 Available at https://centaur.reading.ac.uk/68223/

It is advisable to refer to the publisher's version if you intend to cite from the work. See Guidance on citing.
Published version at: http://dx.doi.org/10.1021/acs.jpcc.6b10023
To link to this article DOI: http://dx.doi.org/10.1021/acs.jpcc.6b10023

Publisher: American Chemical Society

All outputs in CentAUR are protected by Intellectual Property Rights law, including copyright law. Copyright and IPR is retained by the creators or other copyright holders. Terms and conditions for use of this material are defined in the End User Agreement.

www.reading.ac.uk/centaur

University of Reading

CentAUR

Central Archive at the University of Reading

Reading's research outputs online

Adsorption of Methyl Acetoacetate at Ni{111}: Experiment and Theory

Jorge Ontaneda[†], *Richard E. J. Nicklin*[†], *Alix Cornish*[†], *Alberto Roldan*[‡], *Ricardo Grau-Crespo*[*†] *and Georg Held*[*†§]

[†] Department of Chemistry, University of Reading, Whiteknights, Reading RG6 6AD, UK.

*Emails: r.grau-crespo@reading.ac.uk; g.held@reading.ac.uk

[‡] School of Chemistry, Cardiff University, Main Building, Park Place, Cardiff CF10 3AT, UK

[§] Diamond Light Source Harwell Science and Innovation Campus, Didcot OX11 0QX, UK

(November 7, 2016)

Abstract. The hydrogenation of methyl acetoacetate (MAA) over modified Ni catalysts is one of the most important and best studied reactions in heterogeneous enantioselective catalysis. Yet, very little molecular-level information is available on the adsorption complex of the reactant. Here we report on a combined experimental and theoretical study of MAA adsorption on Ni{111}. XPS shows that the chemisorbed layer is stable up to 250 K; above 250 K decomposition sets in. In ultra-high vacuum conditions, multilayers grow below 150 K. DFT modelling predicts a deprotonated enol species with bidentate coordination on the flat Ni{111} surface. The presence of adatoms on the surface leads to stronger MAA adsorption in comparison with the flat surface, whereby the stabilization energy is high enough for MAA to

drive the formation of adatom defects at Ni{111}, assuming the adatoms come from steps. Comparison of experimental XPS and NEXAFS data with theoretical modeling, however, identify the bidentate deprotonated enol on the flat Ni{111} surface as the dominant species at 250 K, indicating that the formation of adatom adsorption complexes is kinetically hindered at low temperatures.

1. INTRODUCTION

Research into enantioselective catalysis of bio-related molecules dates back to the 1960s with much of the early work carried out by Izumi et al. on the hydrogenation of *β*-keto esters over modified Raney nickel catalysts.[1,2] The last two decades have seen dramatic developments in the quantitative molecular-scale characterization and the understanding of chiral and chirally-modified surfaces of model catalysts. This progress has been driven by the growing demand for optically pure chemicals in drug manufacturing, as well as by the refinement of experimental surface characterization techniques and theoretical methods of modelling adsorption and surface reactions.[3–6] Heterogeneous catalysts avoid the problem of phase separation that is inherent in homogeneous catalytic processes, which are predominantly used today.[7] Therefore, viable heterogeneous routes for enantio-pure building blocks of pharmaceuticals and other fine chemicals would make their production significantly greener and more economical.

In the case of the simplest *β*-ketoester, methyl acetoacetate (MAA), the hydrogenation results in a racemic mixture of *R* and *S* methyl-3-hydroxybutyrate (M3HB) when performed with an unmodified Raney Ni catalyst. Modification of the catalyst with *α*-amino or *α*-hydroxy acids, however, can lead to results in high enantiomeric excess, up to 86%. The reaction is well characterized in terms of macroscopic quantities such as enantiomeric excess, temperature and

solvent dependencies.[1,8–10] It has been shown that the solvent has a significant influence on the enantiomeric excess and the corrosion of the catalyst, which indicates that the surface modification is due to a combination modifier and solvent molecules. The large body of work by Izumi *et al.* has also led to the conclusion that the enantioselective behavior depends on how the reactant MAA adsorbs on the Ni surface and how it interacts with the modifier, rather than on the transition state of the hydrogenation reaction. Hence, understanding the adsorption complex of MAA and the influence modifiers have on it is a key step in achieving and optimizing enantioselective behavior of Ni-based catalysts.

Many of the recent surface studies have concentrated on close-packed single crystals of coinage and Pt-group metals. On these surfaces many chiral modifiers and/or reactants form ordered adsorbate layers with well-defined chemical environments under UHV conditions which can be studied by a variety of surface science methods. On Ni surfaces such ordered structures are rare. Therefore, little quantitative molecular-scale information related to the aforementioned hydrogenation reactions is available for modified Ni catalysts. Raval's group have studied stress-induced induction of chirality onto the substrate after adsorption of tartaric acid on Ni{110}.[11–13] The best studied Ni surface is Ni{111} mainly due to the work of Baddeley's group, who have studied the adsorption of MAA and several modifiers, including tartaric acid and glutamic acid, on Ni{111} and polycrystalline Ni, using temperature-programmed desorption, IR spectroscopy, scanning tunnelling microscopy (STM) and X-ray photoelectron spectroscopy (XPS).[10,14–18] Our recent study of alanine on Ni{111} used XPS and near edge X-ray absorption spectroscopy (NEXAFS) to characterize the adsorption geometry of this modifier.[19]

These experimental studies, as well as theoretical work,[11,13,20] show that the behavior of modifier molecules on Ni is very different from that on Cu surfaces[21,22] and more comparable to Pd surfaces in the sense that zwitterionic species are observed, even in chemisorbed layers and the adsorption geometry deviates from the "OON" footprint usually observed on Cu surfaces.[23,24] As far as MAA is concerned, Jones *et al.* found evidence for 1:1 interaction with the chiral modifiers and that the molecule occurs predominantly in its enol tautomeric form when it interacts with the modifiers.[10,15,18] In addition, there has been some recent spectroscopic work on chirally modified polycrystalline and nanoparticulate Ni catalysts which also indicates a variety of chemical species present at the surface and the presence of enol species.[25,26]

Our recent work on the adsorption of chiral modifiers on Ni, Pt and Cu surfaces has shown that the combination of XPS and NEXAFS is very powerful in characterizing the adsorption complex in terms of chemical state, bond coordination and molecular orientation.[19,27–30] These spectroscopies do not depend on long-range order and can even be applied under near-ambient pressure conditions. They are therefore well suited for the study of chiral modifiers and reactants on Ni surfaces. In this work we combine the spectroscopic study of MAA on Ni{111} with DFT modelling in order to gain a more complete characterization of the adsorption complex.

2. METHODOLOGY

2.1. **Experimental Techniques.** XPS and NEXAFS experiments were performed at the UHV endstation of beamline I-311 at the MAXlab Synchrotron Radiation Facility in Lund, Sweden, which is equipped with a Scienta SES-200 electron energy analyzer.[31] Standard procedures including Ar^+ ion sputtering, and annealing to 1000 K in UHV were applied for

sample cleaning. Cleanliness was checked by XPS. The sample temperature was measured by means of a K-type thermocouple spot welded to the sample.

MAA was purified by repeated freeze-thaw cycles. It adsorbed via a micro-channel array doser at a distance of about 2 cm from the sample. The background pressure in the vacuum chamber rose from about 5×10^{-10} mbar to 5×10^{-9} mbar during adsorption but the pressure in front of the sample is estimated to be about an order of magnitude higher.

XP spectra in the C 1s and O 1s regions were recorded using photon energies of 410 eV and 650 eV, respectively, and a pass energy of 50 eV. Spectra of the Fermi edge were measured after each change in the beamline settings with the same monochromator and analyzer parameters (photon energy, pass energy) to calibrate the offset of the binding energies (BE). In order to study the temperature dependence of the absorbed alanine layers, fast XP spectra were recorded at a rate of 20 - 25 s per spectrum while annealing the sample at a constant rate of 0.2 K s^{-1} (4-5 K per spectrum).

NEXAFS spectra at the oxygen K-edge were recorded in Auger-yield mode using the same analyzer as for XPS and with the photon beam at angles of 0° or 65° with respect to the surface normal. The spectra were recorded in the kinetic energy range 490 eV - 525 eV, covering the oxygen KLL Auger emission, while the photon energy was scanned from 525 eV to 555 eV in steps of 0.15 eV. The photon flux, I_0, was recorded by measuring the current from a photodiode inserted into the beamline. NEXAFS spectra were measured for the clean surface and after adsorption of MAA at 180 K and annealing to 250 K. The data presented here are integrated over a smaller kinetic energy range of 505 - 515 eV in order to avoid artificial structures due to photoemission peaks. These spectra are then divided by I_0 and have the clean-surface spectra

subtracted, which were treated in the same way. In a final step, the spectra were normalized with respect to the post-edge (high photon energy) signal at 555 eV.

In order to limit X-ray induced beam damage, the sample was slowly moved across the synchrotron beam during long runs of data acquisition, such as NEXAFS or TP-XPS.

2.2. **Computational Details.** Periodic density functional theory (DFT) calculations were performed with the VASP program.[32,33] As in previous DFT investigations of molecular adsorption at this surface,[34,35] the Ni{111} surface was modeled with a periodic slab consisting of 4 atomic layers, which is known to lead to well converged results for adsorption energies and geometries.[36] Only the two uppermost Ni layers were fully relaxed, while the two bottom layers were fixed in the bulk positions; this procedure is often found to accelerate the convergence of calculated surface properties with respect to the thickness of the simulation slab.[37,38] A vacuum space of 12 Å separates the slabs. Laterally, the supercell consisted of 5×5 surface unit cells. The positions of the MAA molecule were also allowed to fully relax. In order to compensate for the use of an asymmetric slab, all simulations included a dipole correction as implemented in VASP, based on a method proposed by Makov and Payne.[39]

We used a functional based on the generalized gradient approximation (GGA) in the form of the revised Perdew-Burke-Ernzerhof (revPBE) exchange-correlation functional.[40] To correctly account for van der Waals (vdW) interactions, we used the DFT-D3 method with Becke-Jonson (BJ) damping.[41,42] This combination of functional and dispersion correction has been shown by Goerigk and Grimme to provide a very robust description of vdW effects in comparison with other GGA-based formulations.[43] Since nickel is a ferromagnetic metal, all calculations allowed for spin polarization. The projected augmented wave (PAW) method[44,45] was used to describe the

interaction between the valence and core electrons. The number of plane waves in the slab calculations was set by a kinetic energy cutoff of 400 eV, which is the recommended value for the employed PAW potentials. Monkhorst-Pack grids[46] with a maximum separation of 0.15 $Å^{-1}$ between *k*-points were used for sampling the Brillouin-zone. This grid density, which was checked with respect to convergence of the Ni bulk total energy, corresponds to a 4×4×1 grid for the reciprocal space of the slab model. Isolated molecules of MAA in the gas phase were simulated using a large cage which ensures that periodic replicates are separated by at least 13 Å. Ionic positions were relaxed using a conjugated gradient algorithm until the forces on atoms were all less than 0.02 $eVÅ^{-1}$.

We explored the configurational space of adsorption by performing energy minimizations starting from all sensible initial positions of the MAA molecule with respect to the surface, and considering both tautomeric forms of the molecule as well as its deprotonated form. For each final stable adsorption configuration, we calculated the adsorption energy (E_{ads}) as follows:

$$E_{\mathrm{ads}} = E_{\mathrm{slab+mol}} - (E_{\mathrm{slab}} + E_{\mathrm{mol}}) \quad (1)$$

where $E_{slab+mol}$ represents the energy of the optimized substrate-adsorbate system, E_{slab} corresponds to the energy of the relaxed clean Ni{111} surface, and E_{mol} denotes the energy of the MAA molecule in the gas phase, in the lowest-energy tautomeric configuration.

In order to compare with XPS data, we have calculated core-level shifts in the so-called final-state approximation,[47] where the shifts are obtained as total energy differences between two separate calculations.[48] The first one is a standard DFT calculation performed on the fully relaxed system. In the second calculation, one electron from the chosen core level of a specific atom is excited to the lowest conduction band state, allowing only the valence electronic

structure to be relaxed (at fixed geometry). The total energy difference between the two calculations is an estimate of the core-level binding energy, without taking into account the effect of core-electron screening (although screening by valence electrons is included). The method is not able to yield absolute values for the core level binding energies,[48] and in any case, the calculation of such absolute values from DFT is fundamentally problematic.[49] Thus it is common to consider core level *shifts* (E_{CLS}), which can be defined as the variation in binding energy of specific core-electrons (E_{CL}) of atoms compared to reference atoms ($E_{\mathrm{CL}}^{\mathrm{ref}}$):

$$E_{\mathrm{CLS}} = E_{\mathrm{CL}} - E_{\mathrm{CL}}^{\mathrm{ref}} \quad (2)$$

Here, we are mainly interested in the relative shifts of the core levels of different O atoms in the MAA molecule when interacts with the Ni{111} surface; therefore, the choice of reference is irrelevant. Previous work has shown that this computational methodology gives relative core level shifts in excellent agreement with experiment.[48,50,51]

3. RESULTS

3.1. **X-Ray Photoelectron Spectroscopy measurements.** The C 1s and O 1s spectra shown in **Figure 1** were recorded after successive dosing of MAA onto the Ni{111} surface. The background pressure during dosing was 5×10^{-9} mbar but it is estimated that the pressure in front of the sample was about an order of magnitude higher. For the first 6 dosing steps the sample temperature was kept at 180 K. The spectra clearly indicate that the MAA layer saturates at this temperature; after 2 min the integrated O 1s signal intensity is already 85 % of the saturation coverage (after 9 min). O 1s spectra for the saturated layer were also recorded with higher photon energy, 950 eV, for which photoelectron diffraction effects play a minor role. Comparing

the integrated peak area of this spectrum with that of a saturated CO layer (coverage 0.57 ML) measured under the same conditions, leads to an estimated saturation coverage of 0.13 ML, i.e. approximately 1 MAA molecule per 8 Ni surface atoms. This agrees well with the size of a flat-lying chemisorbed molecule (see below).

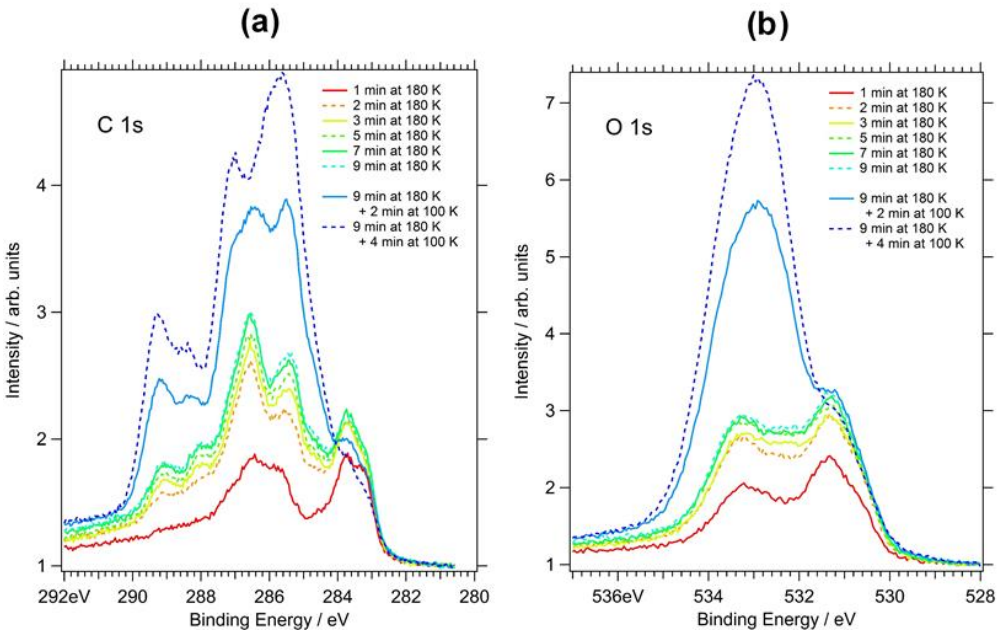

Figure 1. C1s (a) and O 1s (b) spectra recorded after successive dosing steps of MAA onto Ni{111} at 180 K (first 6 spectra) and 100 K (last two spectra). The times indicated in the diagrams are the cumulative dosing times. (Photon energies 410 eV for C 1s and 650 eV for O 1s).

The O 1s spectra of the chemisorbed layer show two clearly resolved peaks at 531.2 eV and 533.1 eV, with the low-BE peak higher in intensity. The C 1s spectra are more complicated with resolvable features at 283.3, 283.8, 285.5, 286.6, 288.0, and 289.1 eV. The two low-BE peaks are probably due to dissociation products formed upon adsorption, as they are similarly seen for alanine adsorbed on the same surface.[19] The most prominent peaks in the saturated layer are at 285.5 eV and 286.6 eV. These are assigned to the C–**C**H–C and the C–**C**H3 (286.6 eV) and O-

CH3 / C=C (285.5 eV). The peak at 288.0 eV is assigned to –**C**OOCH3[25] whereas the origin of the peak at 289.0 eV is unclear, it could be due to small amounts of molecules in the second layer, as this feature becomes more prominent for multilayers.

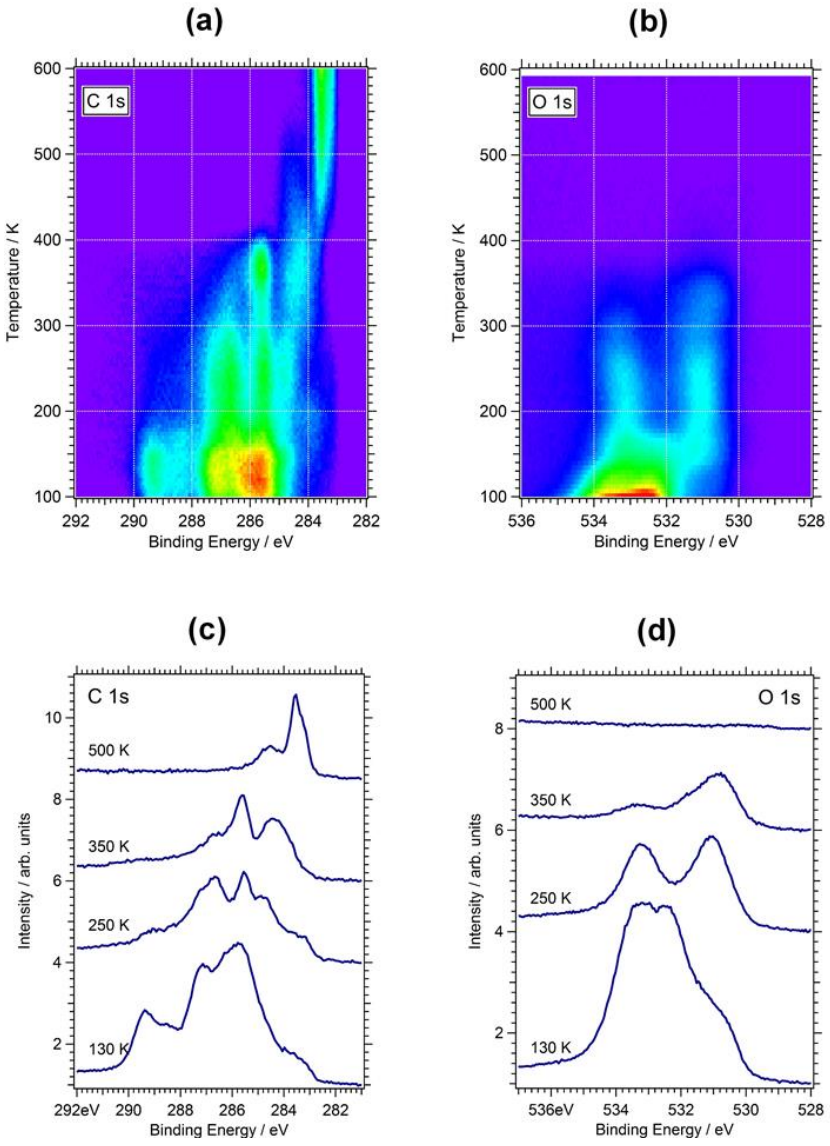

Figure 2. Temperature-programmed (TP-) XPS plots in the C 1s (a) and O 1s (b) regions for approximately 0.25 ML MAA dosed at 100 K and 130 K respectively. The false colors correspond to the photoemission intensity. Bottom panel: selected C1s (c) and O 1s (d) spectra for characteristic temperatures. (Photon energies 410 eV for C 1s and 650 eV for O 1s).

For the last two dosing steps the sample temperature was lowered to 100 K. The corresponding spectra in **Figure 1** show a massive increase in the peak intensity (225% of saturation coverage at 180 K after 4 min) and a general shift towards higher binding energies, especially in the O 1s spectra. This is typical for multilayer growth.

Figure 2 shows temperature-programmed (TP-) XPS plots for the C 1s and O 1s signals of layers of approximately 0.25 ML MAA (i.e. chemisorbed layer plus one condensed layer) dosed at 100 K and 130 K, respectively. The graphs clearly show several transitions in the molecular layers as the sample temperature increases: The onset of multilayer desorption occurs at 150 K. The chemisorbed layer is stable up to about 270 K. Above this temperature the O 1s signal decreases continuously up to 390 K, where it has completely disappeared. In the same temperature window, the C 1s TP-XPS plot shows strong features appearing at 285.6 eV and 284.4 eV, which indicate decomposition products. The feature at 285.6 eV disappears at 400 K, while the low BE feature gradually converts into a strong peak at 283.5 eV, which is typical for atomic (carbidic) carbon on Ni{111}. The conversion is completed at 550 K.

3.2. **NEXAFS.** The O K-edge NEXAFS spectra shown in **Figure 3** were recorded from a saturated chemisorbed layer of MAA dosed at 130 K, followed by annealing to 250 K in order to improve molecular ordering. Auger-yield intensities were recorded at 200 K with the synchrotron beam at normal incidence (0°) and 65° off normal incidence. The strong π resonance is composed of two peaks at 530.9 eV and 532.2 eV, which is especially obvious in the data for 65°. Both peaks show strong angular dependence. Their peak positions and heights were determined by a simultaneous fit of both spectra involving 4 Gaussian functions (2 for the π resonance and 2 for the σ resonances above 535 eV) and a step function at 533.1 eV. In addition

to the data and overall fits to the spectra (solid / dashed lines), **Figure 3** also shows the two individual Gaussians of the π resonance, the step function, and the sum of the two Gaussians used to fit the spectra above 535 eV. Note that some details in the upper energy range are not well reproduced by only two Gaussians. However, this does not affect the quantitative analysis of the π resonance, which we are concentrating on here.

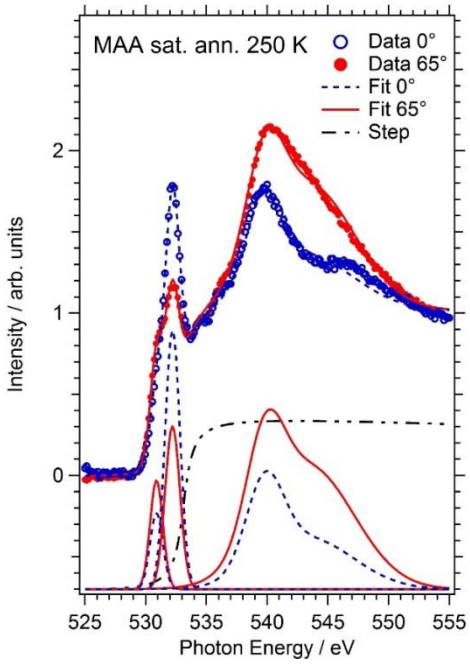

Figure 3. O K-edge NEXAFS spectra for a saturated chemisorbed layer of MAA dosed at 130 K, followed by annealing to 250 K.

The π resonances around 531-533 eV are usually associated with keto C=O double bonds or metal-bonded de-protonated C-O single bonds, which also exhibit some π characteristics.[52] The ratios of these peaks at 0° and 65°, I(0°)/ I(65°), are 0.698 at 530.9 eV and 1.59 at 532.2 eV. According to the formula given by Stöhr and Outka for 3-fold symmetric substrates,[53] this corresponds to C=O bond angles of 49 ± 1° and 62.5 ± 1° with respect to the surface plane.

3.3. **DFT simulation of gas-phase MAA.** As a starting point for the DFT simulation of the adsorption of MAA on Ni{111}, we have calculated the isolated molecule in vacuum in different tautomeric forms and conformations. MAA is a non-symmetrically substituted *β*–diketone containing both CH_3 and OCH_3 substitutions. Symmetrically substituted *β*–diketones exist in the enol tautomeric form R-C(OH)-CH-C(O)-R when R is CH_3, and in the diketo tautomeric form R-C(O)-CH_2-C(O)-R when R is OCH_3.[54] The presence of both CH_3 and OCH_3 in MAA makes its tautomeric behavior particularly interesting. Experimental studies based on gas electron diffraction (GED) and IR (matrix) spectroscopy have shown a mixture of 80% enol and 20% diketo form in MAA vapor at 309K.[55] However, according to ^{1}H NMR spectra and ^{13}C NMR spectra at room temperature, liquid MAA exists exclusively in the diketo form.[56] The crystal structure also exhibits only the diketo tautomer.[57]

We calculated the two tautomeric forms of the isolated molecule, considering also different conformations. **Figure 4** shows the three most stable structures found in our study. As expected from experiment, the most stable structure in the gas phase corresponds to the enol tautomer, with the hydroxyl adjacent to the CH_3 group (the other configuration, with the hydroxyl adjacent to the OCH_3 group, is considerably less stable, by 1.2 eV). The geometry optimization of the enol tautomer leads to a "planar" structure, where all the oxygen atoms are contained in the plane defined by the three carbon atoms (**Figure 4a**). Previous quantum chemical calculations at B3LYP and MP2 level have led to similar results.[55] As shown in **Table S1** of the **Supporting Information**, the computed geometry of the enol tautomer agrees well with that obtained from the GED experiment: the discrepancies in inter-atomic distances are all within ~1%.

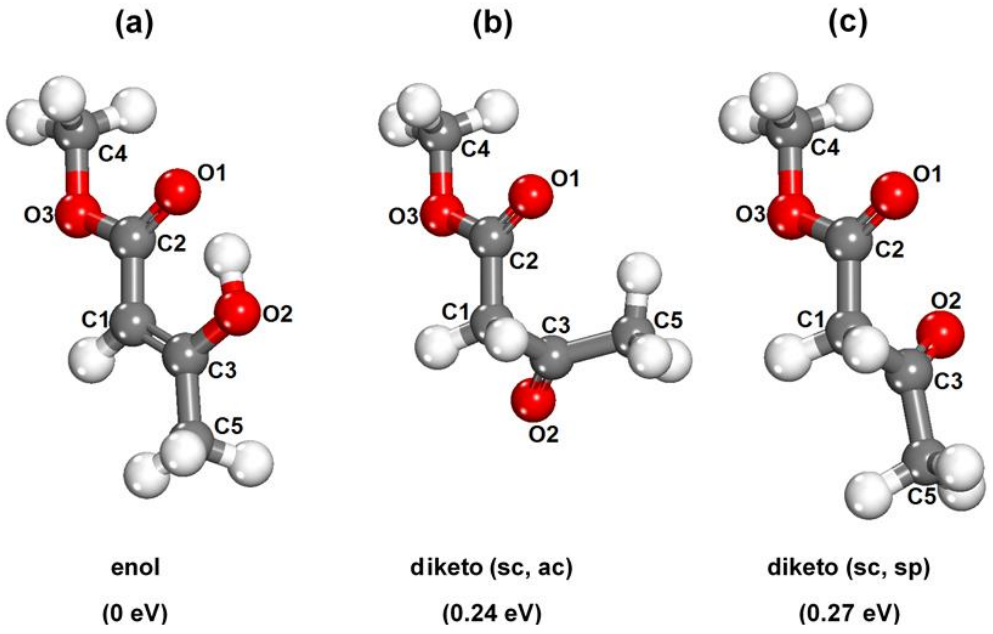

Figure 4. Molecular structures of the two MAA tautomers: (a) enol and (b,c) diketo in two different conformations. The terms "ac", "sc" and "sp" stand for anticlinal, synclinal and synperiplanar respectively

For the diketo tautomer the two most stable conformers (**Figure 4b,c**) have similar energies (0.24 eV and 0.27 eV above the enol groundstate). **Table S2** of the **Supporting Information** lists the geometrical parameters of these two MAA conformers, in comparison with the experimental values for the diketo molecule in the crystal structure.[57] The main difference between the two theoretical diketo structures is in the dihedral angle ∠(C2C1C3O2), which makes the *d*(C4–C5) distance in diketo (sc, ac) shorter than its counterpart by 0.95 Å. The crystal structure of MAA at 150 K contains discrete molecules,[57] whose geometrical configuration is very similar to diketo (sc, sp). Since our calculations predict that the diketo (sc, ac) conformer is only slightly more stable than the diketo (sc, sp) conformer (in the gas phase), our result is not in disagreement with the experimental observation for the solid: the intermolecular interactions apparently stabilize the diketo (sc, sp) over the diketo (sc, ac) form. Because the enol form is the

most stable tautomer, we use it as the reference for the calculation of adsorption energies (**Equation 1**) regardless of the mode of adsorption.

3.4. **DFT simulation of MAA adsorption on a flat Ni{111} surface.** We obtained several local minima for the adsorption of MAA at the Ni{111} surface. The two most stable configurations are shown in **Figure 5a,b**. The global minimum corresponds to the *bidentate deprotonated* configuration shown in **Figure 5a**, where the MAA molecular plane is tilted with respect to the surface, to which it is bonded via two carbonyl groups: one (adjacent to CH_3) on a hollow-fcc site and the other (adjacent to OCH_3 group) on an atop site. The dissociated hydrogen atom is adsorbed elsewhere on the surface, preferentially on an fcc site (the same adsorption mode, but with the hydrogen adsorbed on an hcp site, is 9 meV higher in energy). This adsorption configuration of the molecule can be designated as enol, even if the H atom is not there: a bond with the surface is formed instead, and the C=C double bond remains, i.e. *d*(C1–C3) is 1.376 Å.

Figure 5 (b) shows the lowest-energy geometry for the enol tautomer of MAA adsorbed on the flat Ni{111} surface. In this case, the molecular plane is parallel to the surface with all three oxygen atoms above atop sites. This adsorption geometry (*flat enol*) involves significant vdW interactions between the molecule and the surface. Other stable, higher-energy configurations in the form of enol-MAA are shown in the **Supporting Information (Figure S1)**. Configurations that involve diketo-MAA (**Figure S2**) are less stable by at least 0.5 eV compared with the flat enol geometry.

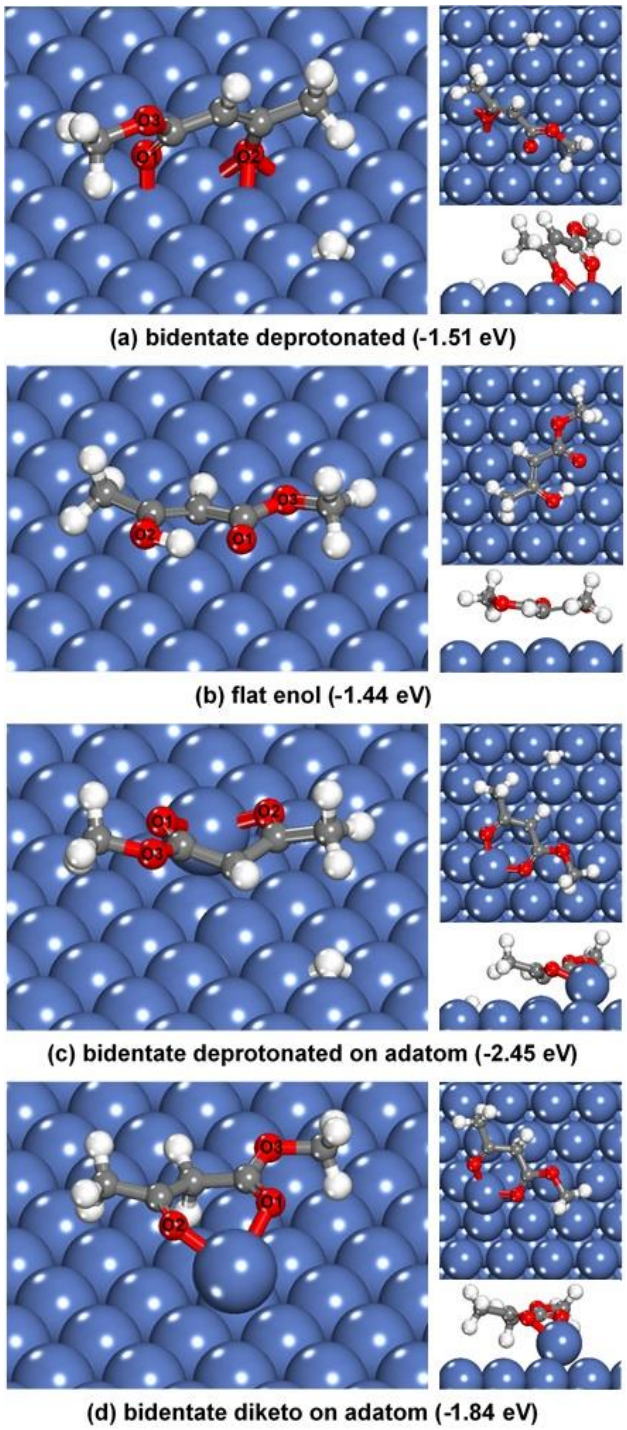

Figure 5. The four lowest-energy configurations of adsorption of MAA at the Ni{111} surfaces. Red atoms correspond to oxygen atoms, grey to carbon atoms and white to hydrogens. Oxygen atoms are numbered in line with Figure 4 and with the discussion of core level shifts below.

3.5. **DFT simulation of MAA adsorption at the adatoms on Ni{111}.** Early theoretical work using the classical embedded-atom method (EAM) calculated a low activation energy (56 meV) for migration of Ni adatom at the Ni{111} surface,[58] which suggests that adatoms which formed, for example, by detachment from surface edges will be very mobile and readily available for the adsorption of molecules. The potentially important role of metal adatoms on molecular adsorption at metal surfaces has been highlighted in more recent studies.[59] Therefore, we have also investigated here the adsorption of MAA at Ni adatoms on Ni{111}. In the simulations presented below, the adatom was located at an fcc site at the surface, which is slightly more stable than the hcp site (difference in defect formation energy is less than 10 meV, see **Ni{111} surface with adatoms** section in the **Supporting Information** for details).

Two different stable configurations for the MAA molecule on the adatom have been found, in which MAA interacts with the Ni adatom via the carboxylic groups. In both cases, the molecular plane is almost parallel to the Ni{111} surface (see **Figure 5c,d**). In the first "*bidentate deprotonated on adatom*" configuration (**Figure 5c**), with an adsorption energy of -2.45 eV, MAA is deprotonated with the dissociated hydrogen atom adsorbed at an fcc site. This is 18 meV lower in energy than H adsorption on the hcp site with the same MAA-Ni adsorption complex. The second more stable adatom complex "*bidentate diketo on atatom*", shown in **Figure 5d,** is less stable than the previous one by more than 0.6 eV. This is the only diketo adsorption configuration found in our calculations, and is unlikely to compete with the stronger adsorption mode in the presence of adatoms. This is interesting, since previous experimental work on co-adsorption of glutamate and MAA on Ni{111} suggested that the MAA was adsorbed in a parallel geometry in the diketo form at 300K.[18]

In order to compare the adsorption energies on the flat surface with those on the adatom, we should take into account that the latter do not include the energy cost of creating the adatom in the first place. The formation energy (E_f) of the adatom was evaluated in two scenarios: (a) formation from a step edge, leaving an edge vacancy behind (b) formation from the flat terrace, leaving a terrace vacancy (see **Figure S3** in **Supporting Information**). As expected, scenario (a) leads to much lower formation energy ($E_f^{(a)}$ = 0.19 eV) than scenario (b) ($E_f^{(b)}$ =2.26 eV).

Clearly, adding the adatom formation energy from the terrace sites, makes both adatom adsorption configurations unfavorable compared to adsorption directly on the flat terrace. However, if the adatom is formed from a step edge, the overall adsorption energy for the *bidentate deprotonated on adatom* is -2.45 eV + 0.19 eV = -2.26 eV. This means that MAA adsorption can in principle stabilize the adatom formation from a step edge, in a process that is energetically more favorable than direct adsorption at the terrace site with no adatoms involved. Of course, these results only refer to the thermodynamic preference; it is possible that there are kinetic limitations for the edge-to-adatom mechanism, especially at the high MAA coverages of interest here. It is therefore difficult to predict, from energy calculations only, what the predominant mode of adsorption is, and whether or not it involves Ni adatoms. We need to resort to the comparison of the experimental XPS spectra with the simulated spectra for the different adsorption configurations.

Table 1. Key geometrical and spectroscopic parameters of the candidate structures with the lowest adsorption energies found by DFT. The parameter Δz is the maximum difference in height of the molecule's carbon atoms with respect to the surface. Core-level binding energy shifts (E_{CLS}) for oxygen atoms on both surfaces. Only relatives shift of O 1s are given according to Equation 2. For numbering refer to Figure 4.

	Bidentate deprotonated	**Flat enol**	**Bidentate deprotonated on adatom**	**Bidentate diketo on adatom**
E_{ads} (eV)	-1.51	-1.44	-2.45 (-2.26)	-1.84 (-1.65)
d(C2–O1) (Å)	1.262	1.256	1.258	1.243
d(C3–O2) (Å)	1.343	1.336	1.279	1.251
∠C2O1surface (degrees)	47.8	11.2	6.4	7.4
∠C3O2surface (degrees)	61.5	5.0	2.7	10.1
Δz (Å)	0.733	0.621	1.057	0.482
ΔBE (O1) (eV)	0.00	0.00	0.33	0.60
ΔBE (O2) (eV)	0.38	1.44	0.00	0.00
ΔBE (O3) (eV)	1.96	1.96	2.16	2.55

3.6. **Calculation of core level bindings energy shifts.** In order to compare the compare the above candidate structures with experimental XPS data, we performed core-level shift calculations for the O 1s photoemission levels according to **Equation 2**. The results are summarized in **Table 1** together with some key geometrical data. In all four cases the binding energy shifts split into two groups around ΔBE = 0.0 – 0.6 eV and ΔBE = 1.4 - 2.5 eV. With the exception of the "flat enol" configuration, the two oxygen atoms from the carboxylic groups (O1 and O2) are characterized by the lower BE. The oxygen atom of the OCH_3 group (O3) always leads to a high BE.

4. DISCUSSION

For a better comparison of the calculated chemical shifts with the experimental O 1s XPS data, spectra were modelled by the sum of three Gaussians centered at the calculated BE shifts. For each Gaussian a width (FWHM) of 1.4 eV was used, which is the smallest width measured for the experimental O 1s peaks. These model spectra are plotted in **Figure 6** together with the experimental O 1s spectrum of MAA at 53 % of saturation coverage (0.07 ML / 1 MAA per 15 Ni atoms) dosed at 180 K. This spectrum has been chosen for comparison as the coverage is closest to the coverage used in the model calculations (1 MAA per 25 Ni atoms). The BE scale of the experimental spectrum has been shifted such that it coincides with the model spectra.

None of the model spectra perfectly matches the peak height ratio of 1.56 : 1 (low BE : high BE), which is to be expected, as attenuation and photoelectron diffraction effects are not incorporated in the model spectra. However, except for that of the flat enol spectrum, all the simulated spectra are in qualitative agreement with the experimental relative peak heights. The energy separation of the two peaks is best reproduced by the two bidentate deprotonated models: ΔBE = 1.8 eV / 2.0 eV for adsorption on the flat surface / Ni adatom while the experimental value is 1.94 eV. Thus, on the ground of the core level shifts we can only exclude the flat enol configuration with reasonable confidence.

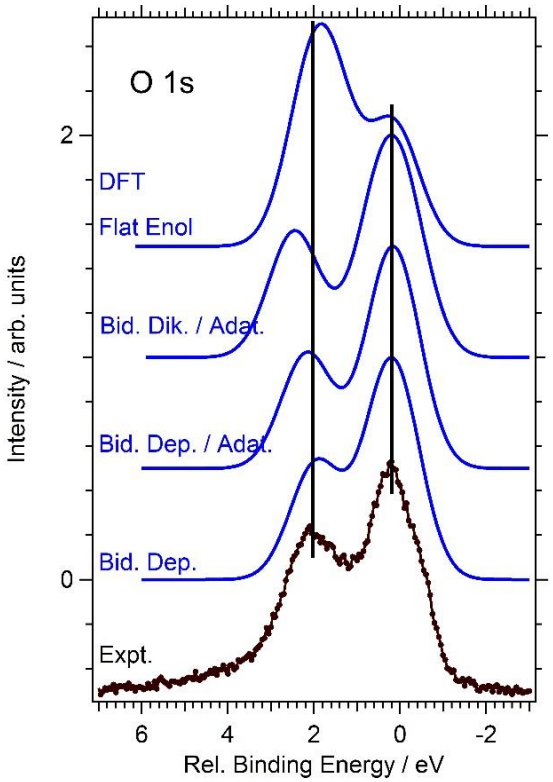

Figure 6. Model O 1s spectra for the MAA geometries that lead to the lowest adsorption energies in the DFT calculations: (top down) flat enol, bidentate diketo on Ni adadom, bidentate deprotonated on Ni adadom, bidentate deprotonated on flat surface. Dots: experimental O 1s spectrum for 0.07 ML MAA dosed at 180 K.

A much clearer discrimination can be achieved from an analysis based on the NEXAFS results and the DFT geometries. The data clearly indicate large C-O bond angles of 49° and 62.5° with respect to the surface plane. These angles are almost exactly reproduced in the DFT simulations by the "*bidentate deprotonated*" configuration without adatom, with values of 47.8° and 61.5°, while all other geometries are characterized by angles of 11.2° or less. We therefore conclude that the molecular adsorption geometry observed in the experiments is in fact "*bidentate deprotonated*". The fact that the adatom geometries are not observed despite their lower adsorption energies as found by DFT modelling can be explained by the low temperatures of 250 K or less, at which the adsorbate layers for Figures 1 and 3 were prepared. Significant

adatom generation from step edges of Ni surfaces, however, takes place well above room temperature.[60] Therefore the formation of adatoms complexes appears to be kinetically hindered. It may well be that the onset of decomposition, which is observed above 250 K, is linked with the increasing availability of single Ni atoms at this temperature.

The bidentate deprotonated geometry has the least "chiral characteristic" of all four candidate structures. If the orientation of the molecular plane was exactly upright hydrogenation should occur from both sides with equal probability. The other geometries with the molecular planes almost parallel offer more obvious pathways to enantioselective hydrogenation of the C=C (or C=O) bond. The surface complexes of the latter structures are "more chiral" and it can be easily envisaged how chiral modifier molecules could stabilize one enantiomer over the other. This mechanism was suggested by Jones and Baddeley in the interaction of MAA with (*S*)-Glutamic Acid modified Ni{111}.[18] The fact, however, that the molecular plane in the bidentate deprotonated geometry actually leans towards one side should also favor one enantiomer over the other. The direction of inclination can be again selected by chiral modifiers.

In this context it is also worth noting that the decomposition temperature observed in our UHV experiments is well below the typical range of reaction temperatures for the enantioselective hydrogenation of MAA on Raney nickel, 333-343 K.[8] Under reaction conditions decomposition may be hindered by the presence of a solvent and/or hydrogen on the surface. In addition, adatoms will also be more readily available which could lead to a change in the adsorption geometry and bond coordination of the adsorption complex.

CONCLUSIONS

In summary, we have performed a combined experimental (XPS and NEXAFS) and theoretical study of MAA adsorbed on Ni{111}. The chemisorbed layer is stable up to 250 K. Above 250 K decomposition occurs, while multilayers grow below 150 K. The NEXAFS data clearly indicate large C=O bond angles of 49° / 62.5° with respect to the surface plane.

Our DFT simulations predict that the MAA enol tautomer is more stable than the diketo tautomer in the gas phase. The preferred adsorption configuration of MAA at the flat Ni{111} surface is a deprotonated species one with bidentate coordination. The adsorption of the non-dissociated enol tautomer is less stable by 77 meV. The presence of adatoms leads to stronger MAA adsorption in comparison with the flat surface, whereby the stabilization energy is high enough for MAA to drive the formation of adatom defects at Ni{111} (assuming the adatoms come from surface steps).

Calculation of oxygen core-level shifts for the theoretical adsorption geometries and comparison with the XPS together with the tilt angles derived from NEXAFS unambiguously identify the bidentate deprotonated enol on the flat Ni{111} surface as the dominant species at 250 K, indicating that the formation of adatom adsorption complexes is kinetically hindered at low temperatures.

SUPPORTING INFORMATION

Additional data from DFT calculations, including comparison of calculated geometries of gas-phase molecules with experiment and information about less stable adsorption configurations not described in the manuscript; file with coordinates for predicted adsorption configuration.

ACKNOWLEDGEMENTS

J.O. acknowledges funding from Ecuador Government's agency SENESCYT in the form of a PhD studentship award (CA-2012-2). The research leading to these results received funding from the UK's EPSRC (EP/G068593/1 and EP/F02116X/1), and the European Commission (FP7/2007-2013) CALIPSO under grant agreement No. 312284. The authors thank the staff of MAXlab for their help during the experiments. This work made use of ARCHER, the UK's national high-performance computing service, *via* the UK's HPC Materials Chemistry Consortium, which is funded by EPSRC (EP/L000202).

REFERENCES

(1) Izumi, Y. Modified Raney Nickel (MRNi) Catalyst: Heterogeneous Enantio-Differentiating (Asymmetric) Catalyst. *Adv. Catal.* **1983**, *32*, 215–271.

(2) Webb, G.; Wells, P. B. Asymmetric Hydrogenation. *Catal. Today* **1992**, *12*, 319–337.

(3) Baiker, A. Progress in Asymmetric Heterogeneous Catalysis: Design of Novel Chirally Modified Platinum Metal Catalysts. *J. Mol. Catal. A Chem.* **1997**, *115*, 473–493.

(4) Baiker, A. Transition State Analogues — a Guide for the Rational Design of Enantioselective Heterogeneous Hydrogenation Catalysts. *J. Mol. Catal. A Chem.* **2000**, *163*, 205–220.

(5) Baddeley, C. J.; Held, G. Chiral Molecules on Surfaces. In *Comprehensive Nanoscience and Technology*; Andrews, D., Scholes, G., Wiederrecht, G., Eds.; Elsevier: Amsterdam, 2010; pp 105–133.

(6) Baddeley, C. J.; Jones, T. E.; Trant, A. G.; Wilson, K. E. Fundamental Investigations of Enantioselective Heterogeneous Catalysis. *Top. Catal.* **2011**, *54*, 1348–1356.

(7) Sharpless, K. B. Searching for New Reactivity (Nobel Lecture). *Angew. Chemie Int. Ed.* **2002**, *41*, 2024–2032.

(8) Keane, M. A. Adsorption of Optically Pure Alanine on Silica-Supported Nickel and the Consequent Catalytic Enantioselectivity. *Langmuir* **1994**, *10*, 4560–4565.

(9) Keane, M. A. Interaction of Optically Active Tartaric Acid with a Nickel−Silica Catalyst: Role of Both the Modification and Reaction Media in Determining Enantioselectivity. *Langmuir* **1997**, *13*, 41–50.

(10) Jones, T. E.; Rekatas, A. E.; Baddeley, C. J. Influence of Modification pH and Temperature on the Interaction of Methylacetoacetate with (S)-Glutamic Acid-Modified Ni{111}. *J. Phys. Chem. C* **2007**, *111*, 5500–5505.

(11) Humblot, V.; Haq, S.; Muryn, C.; Hofer, W. A.; Raval, R. From Local Adsorption Stresses to Chiral Surfaces: (*R*,*R*)-Tartaric Acid on Ni(110). *J. Am. Chem. Soc.* **2002**, *124*, 503–510.

(12) Humblot, V.; Haq, S.; Muryn, C.; Raval, R. (R,R)-Tartaric Acid on Ni(110): The Dynamic Nature of Chiral Adsorption Motifs. *J. Catal.* **2004**, *228*, 130–140.

(13) Hofer, W. A.; Humblot, V.; Raval, R. Conveying Chirality onto the Electronic Structure of Achiral Metals: (R,R)-Tartaric Acid on Nickel. *Surf. Sci.* **2004**, *554*, 141–149.

(14) Jones, T. E.; Baddeley, C. J. A RAIRS, STM and TPD Study of the Ni{111}/R,R-Tartaric

Acid System: Modelling the Chiral Modification of Ni Nanoparticles. *Surf. Sci.* **2002**, *513*, 453–467.

(15) Jones, T. E.; Baddeley, C. J. Direct STM Evidence of a Surface Interaction between Chiral Modifier and pro-Chiral Reagent: Methylacetoacetate on R,R-Tartaric Acid Modified Ni{111}. *Surf. Sci.* **2002**, *519*, 237–249.

(16) Jones, T. E.; Baddeley, C. J. An Investigation of the Adsorption of (R,R)-Tartaric Acid on Oxidised Ni{111} Surfaces. *J. Mol. Catal. A Chem.* **2004**, *216*, 223–231.

(17) Jones, T. E.; Urquhart, M. E.; Baddeley, C. J. An Investigation of the Influence of Temperature on the Adsorption of the Chiral Modifier, (S)-Glutamic Acid, on Ni{111}. *Surf. Sci.* **2005**, *587*, 69–77.

(18) Jones, T. E.; Baddeley, C. J. Investigating the Mechanism of Chiral Surface Reactions: The Interaction of Methylacetoacetate with (S)-Glutamic Acid Modified Ni{111}. *Langmuir* **2006**, *22*, 148–152.

(19) Nicklin, R. E. J.; Cornish, A.; Shavorskiy, A.; Baldanza, S.; Schulte, K.; Liu, Z.; Bennett, R. A.; Held, G. Surface Chemistry of Alanine on Ni{111}. *J. Phys. Chem. C* **2015**, *119*, 26566–26574.

(20) Ghiringhelli, L. M.; Schravendijk, P.; Delle Site, L. Adsorption of Alanine on a Ni(111) Surface: A Multiscale Modeling Oriented Density Functional Study. *Phys. Rev. B* **2006**, *74*, 35437.

(21) Barlow, S. M.; Raval, R. Complex Organic Molecules at Metal Surfaces: Bonding,

Organisation and Chirality. *Surf. Sci. Rep.* **2003**, *50*, 201–341.

(22) Held, G.; Gladys, M. J. The Chemistry of Intrinsically Chiral Surfaces. *Top. Catal.* **2008**, *48*, 128–136.

(23) Mahapatra, M.; Tysoe, W. T. Structure and Decomposition Pathways of D-(−)-Tartaric Acid on Pd(111). *Surf. Sci.* **2014**, *629*, 132–138.

(24) Mahapatra, M.; Burkholder, L.; Devarajan, S. P.; Boscoboinik, A.; Garvey, M.; Bai, Y.; Tysoe, W. T. Formation of Induced-Fit Chiral Templates by Amino Acid-Functionalized Pd(111) Surfaces. *J. Phys. Chem. C* **2015**, *119*, 3556–3563.

(25) Wilson, K. E.; Baddeley, C. J. XPS Studies of the Effects of Modification pH on the Interaction of Methylacetoacetate with (S)-Aspartic Acid-Modified Ni Surfaces. *J. Catal.* **2011**, *278*, 41–49.

(26) Watson, D. J.; Acharya, S.; Nicklin, R. E. J.; Held, G. Observing the in Situ Chiral Modification of Ni Nanoparticles Using Scanning Transmission X-Ray Microspectroscopy. *Surf. Sci.* **2014**, *629*, 108–113.

(27) Shavorskiy, A.; Eralp, T.; Schulte, K.; Bluhm, H.; Held, G. Surface Chemistry of Glycine on Pt{111} in Different Aqueous Environments. *Surf. Sci.* **2013**, *607*, 10–19.

(28) Eralp, T.; Shavorskiy, A.; Held, G. The Adsorption Geometry and Chemical State of Lysine on Cu{110}. *Surf. Sci.* **2011**, *605*, 468–472.

(29) Eralp, T.; Ievins, A.; Shavorskiy, A.; Jenkins, S. J.; Held, G. The Importance of Attractive Three-Point Interaction in Enantioselective Surface Chemistry: Stereospecific Adsorption

of Serine on the Intrinsically Chiral Cu{531} Surface. *J. Am. Chem. Soc.* **2012**, *134*, 9615–9621.

(30) Baldanza, S.; Cornish, A.; Nicklin, R. E. J.; Zheleva, Z. V.; Held, G. Surface Chemistry of Alanine on Cu{111}: Adsorption Geometry and Temperature Dependence. *Surf. Sci.* **2014**, *629*, 114–122.

(31) Nyholm, R.; Andersen, J. N.; Johansson, U.; Jensen, B. N.; Lindau, I. Beamline I311 at MAX-LAB: A VUV/soft X-Ray Undulator Beamline for High Resolution Electron Spectroscopy. *Nucl. Instruments Methods Phys. Res. A* **2001**, *467*, 520–524.

(32) Kresse, G.; Furthmüller, J. Efficiency of Ab-Initio Total Energy Calculations for Metals and Semiconductors Using a Plane-Wave Basis Set. *Comput. Mater. Sci.* **1996**, *6*, 15–50.

(33) Kresse, G.; Furthmüller, J. Efficient Iterative Schemes for Ab Initio Total-Energy Calculations Using a Plane-Wave Basis Set. *Phys. Rev. B* **1996**, *54*, 11169–11186.

(34) Remediakis, I. N.; Abild-Pedersen, F.; Nørskov, J. K. DFT Study of Formaldehyde and Methanol Synthesis from CO and H_2 on Ni(111). *J. Phys. Chem. B* **2004**, *108*, 14535–14540.

(35) Mohsenzadeh, A.; Bolton, K.; Richards, T. DFT Study of the Adsorption and Dissociation of Water on Ni(111), Ni(110) and Ni(100) Surfaces. *Surf. Sci.* **2014**, *627*, 1–10.

(36) Wang, S.-G.; Cao, D.-B.; Li, Y.-W.; Wang, J.; Jiao, H. Chemisorption of CO_2 on Nickel Surfaces. *J. Phys. Chem. B* **2005**, *109*, 18956–18963.

(37) O'Rourke, C.; Bowler, D. R. DSSC Anchoring Groups: A Surface Dependent Decision. *J.*

Phys. Condens. Matter **2014**, *26*, 195302.

(38) Tillotson, M. J.; Brett, P.; Bennett, R. A.; Grau-Crespo, R. Adsorption of Organic Molecules at the TiO_2(110) Surface: The Effect of van Der Waals Interactions. *Surf. Sci.* **2015**, *632*, 142–153.

(39) Makov, G.; Payne, M. Periodic Boundary Conditions in Ab Initio Calculations. *Phys. Rev. B* **1995**, *51*, 4014–4022.

(40) Zhang, Y.; Yang, W. Comment on "Generalized Gradient Approximation Made Simple." *Phys. Rev. Lett.* **1998**, *80*, 890–890.

(41) Grimme, S.; Antony, J.; Ehrlich, S.; Krieg, H. A Consistent and Accurate Ab Initio Parametrization of Density Functional Dispersion Correction (DFT-D) for the 94 Elements H-Pu. *J. Chem. Phys.* **2010**, *132*, 154104.

(42) Grimme, S.; Ehrlich, S.; Goerigk, L. Effect of the Damping Function in Dispersion Corrected Density Functional Theory. *J. Comput. Chem.* **2011**, *32*, 1456–1465.

(43) Goerigk, L.; Grimme, S. A Thorough Benchmark of Density Functional Methods for General Main Group Thermochemistry, Kinetics, and Noncovalent Interactions. *Phys. Chem. Chem. Phys.* **2011**, *13*, 6670–6688.

(44) Blöchl, P. E. Projector Augmented-Wave Method. *Phys. Rev. B* **1994**, *50*, 17953–17979.

(45) Kresse, G.; Joubert, D. From Ultrasoft Pseudopotentials to the Projector Augmented-Wave Method. *Phys. Rev. B* **1999**, *59*, 1758–1775.

(46) Monkhorst, H. J.; Pack, J. D. Special Points for Brillouin-Zone Integrations. *Phys. Rev. B* **1976**, *13*, 5188–5192.

(47) Birgersson, M.; Almbladh, C.-O.; Borg, M.; Andersen, J. Density-Functional Theory Applied to Rh(111) and CO/Rh(111) Systems: Geometries, Energies, and Chemical Shifts. *Phys. Rev. B* **2003**, *67*, 45402.

(48) Köhler, L.; Kresse, G. Density Functional Study of CO on Rh(111). *Phys. Rev. B* **2004**, *70*, 165405.

(49) Pueyo Bellafont, N.; Bagus, P. S.; Illas, F. Prediction of Core Level Binding Energies in Density Functional Theory: Rigorous Definition of Initial and Final State Contributions and Implications on the Physical Meaning of Kohn-Sham Energies. *J. Chem. Phys.* **2015**, *142*, 214102.

(50) Gotterbarm, K.; Luckas, N.; Höfert, O.; Lorenz, M. P. A.; Streber, R.; Papp, C.; Viñes, F.; Steinrück, H. P.; Görling, A. Kinetics of the Sulfur Oxidation on Palladium: A Combined in Situ X-Ray Photoelectron Spectroscopy and Density-Functional Study. *J. Chem. Phys.* **2012**, *136*, 094702.

(51) Ontaneda, J.; Bennett, R. A.; Grau-Crespo, R. Electronic Structure of Pd Multilayers on Re(0001): The Role of Charge Transfer. *J. Phys. Chem. C* **2015**, *119*, 23436–23444.

(52) Francis, J. T.; Hitchcock, A. P. Distinguishing Keto and Enol Structures by Inner-Shell Spectroscopy. *J. Phys. Chem.* **1994**, *98*, 3650–3657.

(53) Stöhr, J.; Outka, D. A. Determination of Molecular Orientations on Surfaces from the

Angular Dependence of Near-Edge X-Ray-Absorption Fine-Structure Spectra. *Phys. Rev. B* **1987**, *36*, 7891–7905.

(54) Belova, N. V.; Sliznev, V. V.; Oberhammer, H.; Girichev, G. V. Tautomeric and Conformational Properties of β-Diketones. *J. Mol. Struct.* **2010**, *978*, 282–293.

(55) Belova, N. V.; Oberhammer, H.; Girichev, G. V. Tautomeric and Conformational Properties of Methyl Acetoacetate, $CH_3OC(O)-CH_2-C(O)CH_3$: Electron Diffraction and Quantum Chemical Study. *J. Phys. Chem. A* **2004**, *108*, 3593–3597.

(56) Schiavoni, M. M.; Di Loreto, H. E.; Hermann, A.; Mack, H.-G.; Ulic, S. E.; Della Védova, C. O. Keto-Enol Tautomerism in β-Ketoesters: $CH_3C(O)CHXC(O)OY$ (X = H, Cl; Y = CH_3, C_2H_5). Vibrational Analyses, NMR Spectra and Quantum Chemical Calculations. *J. Raman Spectrosc.* **2001**, *32*, 319–329.

(57) Shallard-Brown, H. A.; Watkin, D. J.; Cowley, A. R. Meth-yl Acetoacetate at 150 K. *Acta Crystallogr. Sect. E* **2005**, *61*, o2422–o2423.

(58) Liu, C.-L.; Adams, J. B. Diffusion Mechanisms on Ni Surfaces. *Surf. Sci.* **1992**, *265*, 262–272.

(59) Ernst, K.-H. Molecular Chirality at Surfaces. *Phys. Status Solidi B* **2012**, *249*, 2057–2088.

(60) Pearl, T. P.; Sibener, S. J. Spatial and Temporal Dynamics of Individual Step Merging Events on Ni(977) Measured by Scanning Tunneling Microscopy. *J. Phys. Chem. B* **2001**, *105*, 6300–6306.
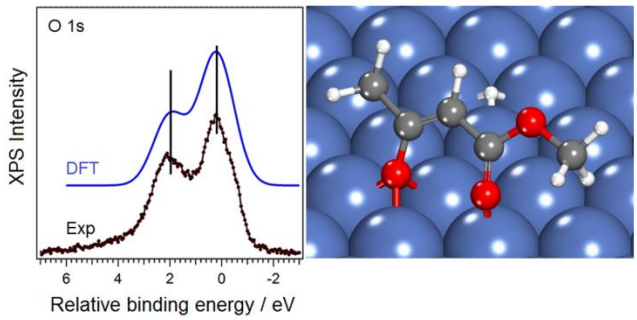
TOC Graphic